Check for updates

3D marine magnetotelluric inversion: A hybrid impedance and direct-field approach

Lutz Mütschard[1], Ketil Hokstad[2], Torgeir Wiik[3], and Bjørn Ursin[1]

ABSTRACT

The measured electromagnetic field in magnetotellurics (MT) is composed of the natural source field and its subsurface response. Commonly, the data are represented as impedances, the complex ratio between the horizontal electric and magnetic fields. This measure is independent of the source distribution because the impedance-tensor estimation contains a deconvolution operator. We have used a Gauss-Newton-type 3D MT inversion scheme to compare impedance-data inversion with an inversion using the recorded electric field directly. The use of the observed electric field is beneficial to the inversion algorithm because it simplifies the estimation of the sensitivities. The direct-field approach permits the use of the observed data without processing, but it presumes knowledge of the source distribution. A method to estimate the time-variable strength and polarization of the incoming plane-wave source is presented and tested on synthetic and real-data examples. The direct-field inversion is successfully applied to a synthetic and a real data set within marine settings. A comparison with the conventional impedance inversion is conducted. The results of the synthetic data example are very similar, with a slightly more accurate reconstruction of the model in the impedance case, whereas the direct-field inversion produces a smoother inversion result when compared with the impedance case. The mapping of a resistive salt structure in the real-data example indicates deviations in the final conductivity models. The impedance inversion suggests a deeper rooted resistive structure, whereas the direct-field inversion predicts a more compact structure limited to the overburden. We have evaluated the advantages of the new approach like the simplification of the sensitivity calculation, limitations, and disadvantages like knowledge of the source distribution.

INTRODUCTION

The 3D modeling and inversion of magnetotelluric (MT) data has made strong progress over the past two decades, leading to diverse implementations of the forward calculation and the inverse model estimation. The papers by Avdeev (2005), Constable and Srnka (2007), and Constable (2010) give a great overview of the advances made by numerous researchers.

Commonly, the observed data input to MT inversions are impedances, in the form of complex tensor elements or apparent resistivities and phases. To our knowledge, little investigation of the data used in the inverse process is published. A Gauss-Newton inversion scheme capable of handling impedances as well as the unprocessed compo-

nents of the electromagnetic (EM) field recorded at the receivers is introduced and used for a comparative study. The motivation for introducing MT inversions of field components is that the inversion scheme becomes less nonlinear and fewer approximations are needed when relating observed data to model parameters.

Soyer and Brasse (2001) invert magnetic interstation transfer functions to study a regional magnetic anomaly in northern Chile. Although the theory of using synchronously recorded geomagnetic data from a reference and many local sites goes back to work of Schmucker (1970), the novel approach was to include this data type into a 2D inversion. Wiik et al. (2013) investigate the joint inversion of marine MT and controlled-source EM data (CSEM), in which the MT data were composed of field components. Because using the

recorded fields directly is common practice in CSEM inversion, we adopted this for the MT data to allow for a joint implementation of the 3D inversion.

The approach by Soyer and Brasse (2001) and the commonly executed impedance inversion share the fact that no information about the source of the exciting EM field is necessary. In CSEM studies, the source is known and is specifically designed to illuminate the target structure. For the joint CSEM MT data inversion, Wiik et al. (2013) use an assumed 1D reference receiver to estimate the factors that scale the EM fields in the forward calculation part of the inversion.

In this study, we introduce a Gauss-Newton-like inversion scheme that can be used with impedance or electric-field data. Because knowledge about of the strength and polarization of the source distribution is necessary to run the direct-field inversion, a methodology to estimate the source scaling factors is derived. The inversion scheme is then applied to two data sets. The first data set contains the synthetic response of a 2D wedge-shaped model with a 3D embedded structure into the wedge slope. The second data set contains observed responses from a marine survey investigating salt structures in the Barents Sea. For both cases, the inversion is run in impedance and direct-field mode. The results from the synthetic and real-data example cases are compared and discussed.

METHOD

Forward calculation

To calculate the components of the EM field from a given isotropic conductivity model, the following equation resulting from the Maxwell equations has to be solved:

$$\nabla \times \nabla \times \mathbf{E} + i\omega\mu_0\sigma\mathbf{E} = -i\omega\mu_0\sigma\mathbf{J}_s, \quad (1)$$

where σ is the scalar electric conductivity, $\mathbf{J}_s$ are the sources of the electric field, ω is the angular frequency, $\mathbf{E}$ is the electric field, and μ_0 is the vacuum magnetic permeability. To avoid irregularities close to the sources of the electric field, a scattered field solution is used. The forward-modeling problem is split into two. The primary field $\mathbf{E}_0$ is composed of a 1D background field modeling, which includes the sources. The secondary field, the deviation from the background field, is called the scattered field $\mathbf{E}'$. Both fields add together to give the total field $\mathbf{E}$

$$\mathbf{E}' = \mathbf{E} - \mathbf{E}_0, \quad (2)$$

where $\mathbf{E}_0$ is the solution of equation 1 in the case $\sigma = \sigma_0$, where σ_0 is the conductivity of the background model. The 1D solution can be calculated analytically. Substituting equation 2 into equation 1, the scattered field formulation becomes

$$\nabla \times \nabla \times \mathbf{E}' + i\omega\mu_0\sigma\mathbf{E}' = -i\omega\mu_0(\sigma - \sigma_0)\mathbf{E}_0. \quad (3)$$

A finite-volume approach is used to solve the Maxwell equations in the frequency domain on a staggered grid. In addition to a finite-difference discretization, conductivities are here integrated over a control volume but the resulting linear system (i.e., equation 5) has the same coefficient matrix for either type of discretization (Weiss and Constable, 2006). The electric field components are placed at the midpoints of the mesh edges and the magnetic field at the face centers of the grid cells. Compared with a finite-difference discre-

tization, integration of the conductivities over a control volume offers additional freedom when constructing the right-hand term of equation 3. To accommodate for MT calculations, the grid spacing increases exponentially toward the edges of the model. The magnetic field is calculated from the electric field solution via Faraday's induction law

$$\nabla \times \mathbf{E} = -i\omega\mathbf{B}. \quad (4)$$

To be efficient, the magnetic field is only calculated at the grid positions surrounding the receiver locations. Equation 3 is solved for the scattered electric field $\mathbf{E}'$ with the help of a direct sparse solver (Schenk and Gärtner, 2004) capable of handling nonregular gridded models. The discretized (finite volume) representation of equation 3 can be written into a linear system of equations

$$\mathbf{Ae} = \mathbf{b}, \quad (5)$$

where $\mathbf{e}$ is a solution vector containing the discrete values of $\mathbf{E}'$, and $\mathbf{b}$ is a boundary value vector. The coefficient matrix $\mathbf{A}$ has 13 nonzero entries per row, all real valued except for a complex value on the diagonal. In case the mesh node spacing is variable, $\mathbf{A}$ becomes nonsymmetric. The coefficient matrix has to be inverted for every frequency and solved with two right sides $\mathbf{b}$, one for each orthogonal source polarizations. The natural source field is variable over time in strength and polarization and can be decomposed into two decoupled terms. The first polarization is often called X - or E-polarization. In a right-handed coordinate system in which the x-axis is pointing north, the y-axis is pointing east, and positive z is pointing downward, the X-polarization describes a southward pointing current system with a negative nonzero E_x- and H_y-component. The second Y- or B-polarization (westward current system) is composed of a negative nonzero E_y and a positive nonzero H_x-component. To simulate MT data, detailed knowledge of these two source terms is innate, and a method to estimate them is given below.

The code for the forward calculation is based on the work of Weiss and Constable (2006). The possibility to scale the primary field and a different solver routine are added to the code.

INVERSION ALGORITHM

The aim of the inverse process is to minimize the following objective function:

$$\phi = \frac{1}{\lambda}[(\mathbf{d} - \mathbf{F}(\mathbf{m}))^T\mathbf{C}_d^{-1}(\mathbf{d} - \mathbf{F}(\mathbf{m}))] + (\mathbf{m} - \mathbf{m}_0)^T\mathbf{C}_m^{-1}(\mathbf{m} - \mathbf{m}_0), \quad (6)$$

with respect to the model $\mathbf{m}$. Here, the leading term describes the misfit between the observed data $\mathbf{d}$ and the predicted data $\mathbf{F}(\mathbf{m})$ from the forward modeling. The function $\mathbf{F}(\mathbf{m})$ includes the forward modeling (estimation of $\mathbf{E}'$ and $\mathbf{E}_0$) and the interpolation of the solution to the receiver positions away from the mesh nodes. The trailing term controls the regularization needed due to the inherent nonuniqueness of the MT inverse problem. The scalar λ weights the data misfit term relative to the regularization term, $\mathbf{d}$ has N elements and $\mathbf{m}$ consists of M conductivities, $\mathbf{C}_d$ is a diagonal matrix containing the data weights, and $\mathbf{C}_m$ is the model covariance matrix that controls the smoothness of the model updates. To allow for the variable roughness in different directions of the inversion

models, the smoothness constraint is implemented by multivariate normal distributions. To stepwise go toward the minimum of ϕ, the following equation is calculated:

$$\mathbf{m}_{k+1} - \mathbf{m}_0 = \mathbf{C}_m \mathbf{J}_k^T (\lambda \mathbf{C}_d + \mathbf{J}_k \mathbf{C}_m \mathbf{J}_k^T)^{-1} (\mathbf{d} - \mathbf{F}(\mathbf{m}_k)$$
$$+ \mathbf{J}_k (\mathbf{m}_k - \mathbf{m}_0)), \qquad (7)$$

where $\mathbf{J}$ is the Jacobi matrix (given by $\mathbf{J} = [\partial \mathbf{F}/\partial \mathbf{m}]$), k is the iteration number, and $\mathbf{m}_0$ is the initial starting model. A complete derivation of this minimum norm scheme can be found in Siripunvaraporn et al. (2005). Note the fact that the approximate data-space Hessian $(\lambda \mathbf{C}_d + \mathbf{J}_k \mathbf{C}_m \mathbf{J}_k^T)$ has only the size of $N \times N$, which helps to speed up the estimation of the normal equation 7. Equation 7 is evaluated for several values of λ. Because negative conductivities are physically not meaningful, we apply a limiter function acting on the model update (i.e., $\mathbf{m}_{k+1}$). A minimum and maximum possible conductivity (0.1 mS/m and 2 S/m are used in the data examples sections below) is defined. The limiter function ensures that all elements of $\mathbf{m}_{k+1}$ lie within the predetermined value range. The λ resulting in the best decrease in data misfit is selected to be used in the calculation of the next iteration model ($\mathbf{m}_{k+1}$). In case no decrease is found, the last model with an improved data misfit is set to be the current reference model ($\mathbf{m}_0$). If a given misfit level is reached, the inversion stops. In case of two resets of $\mathbf{m}_0$, the inversion also stops but can be resumed at a lesser smoothing level (i.e., $\mathbf{C}_m$ is replaced).

The main computational load in our implementation of the inversion is the forward modeling (computing $\mathbf{A}^{-1}$ to solve equation 5 for $\mathbf{e}$) and calculating the model update (equation 7). In the latter case, the estimation of the Jacobi matrix $\mathbf{J}$ is the computationally expensive task. Therefore, once the inverse of $\mathbf{A}$ is found, it is stored in memory and repeatedly used to find the forward solution for the two polarizations and to populate the transposed Jacobian. The sensitivity (Jacobi) matrix quantifies how a small perturbation in the model parameters impacts on the predicted data. Because the reciprocity holds in the MT case, instead of perturbing one model parameter at a time, a series of N (number of data points) pseudo-forward calculations will fully populate the transposed Jacobi matrix, using the following equation:

$$\mathbf{J}^T = \left(-\frac{\partial \mathbf{A}}{\partial \mathbf{m}} \mathbf{e} + \frac{\partial \mathbf{b}}{\partial \mathbf{m}} \right)^T (\mathbf{A}^{-1})^T \left(\frac{\partial \psi}{\partial \mathbf{e}} \right)^T, \qquad (8)$$

where $\mathbf{A}$ is again the coefficient matrix, $\mathbf{b}$ is the boundary values vector, and $\mathbf{e}$ is the scattered electric field solution from equation 3. The term ψ in the trailing factor includes the interpolation to the receiver positions and calculation of the data (Z_{xy}, Z_{yx}, or E_x and E_y) itself. The trailing term acts as a point source at each receiver position, $\mathbf{A}^{-1}$ is known from the forward calculation, and the first term is usually sparse. Because the number of data points in MT is usually a lot smaller than the number of model parameters, this is an efficient method to estimate the sensitivity matrix. A detailed derivation of equation 8 is given in Appendix A. The motivation to directly use field components is given by the great simplification of this term compared with the use of impedances (see Appendix B).

Source estimation

To be able to model the source field present during the recording of the data, the electric field used in the forward calculation has to

vary in strength and polarization for every frequency used in the direct-field inversion. If $e_q^{(j)}(\mathbf{r}, \omega)$ is the horizontal electric field due to a unit source, then two complex source scaling factors $\alpha^{(1)}(\omega)$ and $\alpha^{(2)}(\omega)$ are needed to estimate an electric field $E_q(\mathbf{r}, \omega)$ comparable with the observed one by calculating

$$E_q(\mathbf{r}, \omega) = \alpha^{(1)}(\omega) e_q^{(1)}(\mathbf{r}, \omega) + \alpha^{(2)}(\omega) e_q^{(2)}(\mathbf{r}, \omega), \qquad (9)$$

where the superscript denotes the polarization (i.e., $j = 1, 2$) and the subscript q is either x or y. The function ω is the angular frequency and $\mathbf{r}$ is the receiver position. To be general, $e_q^{(j)}(\mathbf{r}, \omega)$ and $E_q^{(j)}(\mathbf{r}, \omega)$ are related to the magnetic field boundary conditions by

$$e_q^{(j)}(\mathbf{r}, \omega) = -2 \int ds n_i \epsilon_{ijk} G_{qj}^E(\mathbf{r}|\mathbf{r_s}) h_k^{(j)}(\omega), \qquad (10)$$

$$E_q^{(j)}(\mathbf{r}, \omega) = -2 \int ds n_i \epsilon_{ijk} G_{qj}^E(\mathbf{r}|\mathbf{r_s}) H_k^{(j)}(\omega), \qquad (11)$$

where $G_{qj}^E(\mathbf{r}|\mathbf{r_s})$ are the elements of the electric Green's tensors (in 1D, 2D, or 3D), $h_k^{(j)}$ and $H_k^{(j)}$ are the magnetic field components, and ϵ_{ijk} is the Levi-Civita tensor. In general, the Kirchhoff integrals in equations 10 and 11 contain two terms with magnetic and electric field boundary conditions (Mittet et al., 2005). When the direction of the field is known, one boundary condition is sufficient. The factor of two comes from the lack of one boundary condition in the Kirchhoff integral representation of the Maxwell equations for the electric field. The two complex factors $\alpha^{(1)}(\omega)$ and $\alpha^{(2)}(\omega)$ can be found by solving the following linear inverse problem in the least-squares sense:

$$\mathbf{p} = \mathbf{L}\mathbf{q}, \qquad (12)$$

where

$$\mathbf{p} = \begin{bmatrix} E_x(\mathbf{r_1}, \omega) \\ E_y(\mathbf{r_1}, \omega) \\ \dots \\ E_x(\mathbf{r_n}, \omega) \\ E_y(\mathbf{r_n}, \omega) \end{bmatrix} \mathbf{L} = \begin{bmatrix} e_x^{(1)}(\mathbf{r_1}, \omega) & e_x^{(2)}(\mathbf{r_1}, \omega) \\ e_y^{(1)}(\mathbf{r_1}, \omega) & e_y^{(2)}(\mathbf{r_1}, \omega) \\ \dots & \dots \\ e_x^{(1)}(\mathbf{r_n}, \omega) & e_x^{(2)}(\mathbf{r_n}, \omega) \\ e_y^{(1)}(\mathbf{r_n}, \omega) & e_y^{(2)}(\mathbf{r_n}, \omega) \end{bmatrix}$$

$$\times \mathbf{q} = \begin{bmatrix} \alpha^{(1)}(\omega) \\ \alpha^{(2)}(\omega) \end{bmatrix}, \qquad (13)$$

where $\mathbf{p}$ is a $2n \times 1$ matrix of the observed horizontal electric field Fourier coefficients at n receiver locations at a specific frequency and $\mathbf{L}$ is a $2n \times 2$ matrix of the predicted electric field solutions calculated for the two independent source polarizations. A least-squares inversion is used to find the unknown scaling factors using the standard pseudoinverse

$$\mathbf{q} = [(\mathbf{W}\mathbf{L})^T(\mathbf{W}\mathbf{L}) + \lambda \mathbf{S}]^{-1}(\mathbf{W}\mathbf{L})^T(\mathbf{W}\mathbf{p}), \qquad (14)$$

where $\mathbf{W}$ are the data weights and $\mathbf{S}$ can be the identity or the diagonal of the Hessian ($\mathbf{H} = (\mathbf{W}\mathbf{L})^T(\mathbf{W}\mathbf{L})$). Equation 14 is solved for several values of λ.

The scaling factors are selected by forward testing $\alpha^{(1)}$ and $\alpha^{(2)}$ in equation 12. The algorithm used to solve the EM forward problem (equation 3) outputs the fields $\mathbf{E}'$ and $\mathbf{E}_0$ separately for the two source polarizations with a unit source strength ($\alpha^{(1)}, \alpha^{(2)} = 1$) from the final impedance inversion model. Based on misfit, a subselection of receivers is made to find the source field scaling factors that are later input to the field inversion. Examples of this procedure are given in the synthetic and real data section below. In case the data from one or more of the receivers in the survey point to a (for example) 1D subsurface, a simplified source estimation is possible, where the resulting layered inversion model is used for the source scaling. Wiik et al. (2013) uses this 1D method. With the described method to find the source scaling, a preceding impedance model is necessary for the estimation of the source scaling factors. Therefore, the direct-field inversion can be seen as a hybrid method.

The following flowchart (Figure 1) and list summarizes the data preparation steps necessary until right before running the described direct-field inversion:

1) Select raw data: Select a time window of synchronously recorded horizontal electric field time series data.
2) FFT: Transform the time series into the frequency domain.
3) Downward continuation: Unify the low-pass filtering effect of the overlaying seawater for all receivers by a downward field continuation (see Ward and Hohmann, 1988) to the depth of the deepest receiver.
4) Source estimation: Estimate a set of source scaling factors with the help of a 1D, or 3D, model such as described above. It is possible to select a subset of the available receivers to complete this task.
5) Inversion input: Pick a final subset of the electric field Fourier coefficients and source scaling factors of approximately 10–15 frequencies that are used as input data in the inversion.
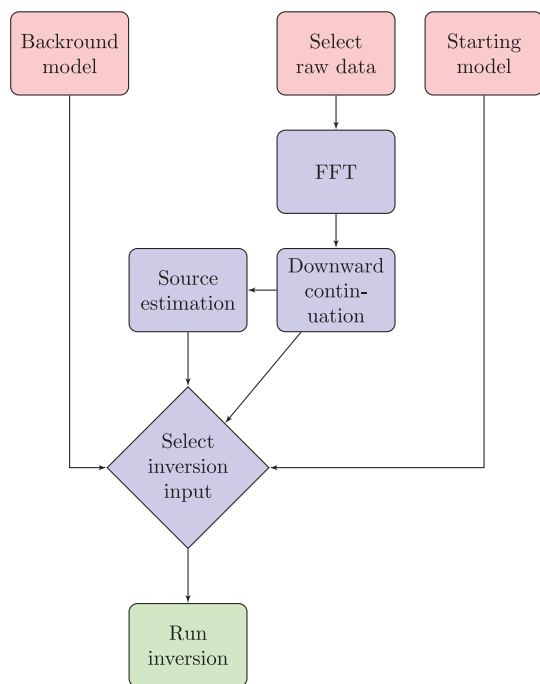
6) Background model: Set up a background model (necessary for the forward calculation). In the current implementation, it consists of three layers (air, water, and lower half-space) and is fixed during the inverse process.
7) Starting model: Set up an initial model including the receiver positions. This conductivity model can be identical to the background model, but it can also, based on prior information, be more detailed. In addition to the starting model conductivities, it is also possible to give prior information by fixing specific model cells and/or set local variable smoothing (i.e., setting $\mathbf{C}_m$).
8) Run: Start the inversion.

DATA EXAMPLE

Synthetic data example

To validate the idea of a direct-field inversion of MT data, the algorithm is first tested on a synthetic data set. The forward model has an overall size of 400 km in the x-direction, 400 km in the y–direction, and 400 km in the z-direction. The model contains 45 mesh nodes in each direction. In the central part (± 9 km), the horizontal mesh resolution is 600 m and decreases toward the outer cells. The vertical size of the model cells increases with depth. The fixed part of the starting model contains four air layers (from $z = -200$ to 0 km) and a 240 m seawater layer with an electric conductivity of 10^{-7} and 3.3 S/m, respectively. To test the capability of the code to reconstruct 3D structures, the test model is composed of a slope over a half-space with an embedded resistive L-structure. Figure 2 shows a map view at 4 km depth, and Figure 3 shows a vertical cut at the $y = 0$ km along the x-axis. The overlaying sediments have a conductivity of 50 mS/m, and the lower half-space has a conductivity of 5 mS/m.

Synthetic data are calculated for 15 periods between 1 and 1000 s at variable source strength (see Table 1). There are 25 receivers with 2400 m distance in the x- and y- directions distributed on the seafloor at a 240 m depth. A 1D model composed of three layers (air, seawater, and basement) with interfaces at depth ($z = 0$ and 240 m), and a basement conductivity of 5 mS/m is used in the forward
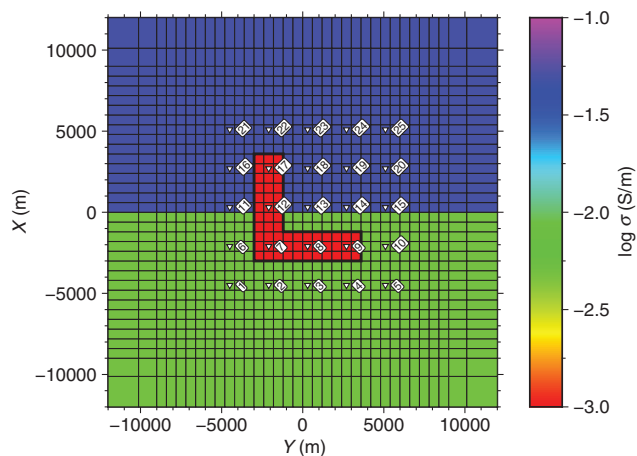

Figure 1. Schematic overview of the preparation steps prior to run the direct-field inversion.

Figure 2. Map view of the model used to create the synthetic data at 4 km depth. White triangles denote receiver positions.

calculation ($\mathbf{E}_0$) as the background model and as the starting model to both inversions (impedance and field). The discretization of the inversion model grid is different from the model used in the calculation of the synthetic data. The inversion model spans 300 km in all directions with $41 \times 41 \times 43$ mesh nodes with a 500 m horizontal and 800 m vertical grid node spacing in the center of the model. Data to both inversions are weighted uniformly with a 5% error, according to the 5% added Gaussian noise. Input to the impedance inversion are the complex off-diagonal elements (Z_{xy}, Z_{yx}) of the impedance tensor at all 25 receivers at 15 frequencies. A unit source strength ($\alpha^{(1,2)} = 1.0$) is used at all iterations.

Figure 4 shows a map view of the inversion model at 4 km depth, and Figure 5 shows a vertical section along the x-axis. The inversion stopped at a root-mean-square (rms) misfit of 1.55 (starting from an initial misfit of 22.5). Because a minimum norm method is used here, the resulting model is a smoothed version of the true model. Nevertheless, a reconstruction of the L-shape and the slope is possible given the coarse model and small amount of data (750 data points).

In the case of real data, the best choice of the background and starting model is not as obvious as in the shown synthetic example. A set of different initial models for two scenarios is used to test their influence on the inversion results. In the first test scenario, the background model (for the scattered-field solver) varies, whereas the starting model (for the inversion) is kept as is. In the second test scenario, the background model is fixed and the starting model varies. The two cases are not identical because the background model is fixed during the inversion, whereas the starting model is changing with every iteration. The first test scenario can also be seen as a simplified way to test how well the forward calculation can cope with situations like bathymetry, or very heterogeneous seafloor resistivities. Five inversions with different conductivities (2, 5, 10, 20, and 100 mS/m) in the basement layer of the background model are executed. In all five inversions, the L-shaped body within the slope is resolved. The inversion with the 20 mS/m lower half-space gives the lowest final misfit, but at the same time introduces conductivity deviations around the L-shaped test body, when compared with the original reference case. The first test case (5 mS/m, i.e., the correct lower half-space) gives a slightly higher misfit but the smoothest model.

The second test investigates the influence of varying starting models on the outcome of the inversion. Again, five different conductivities (2, 5, 10, 20, and 100 mS/m) in the base half-space of the starting model are input to the impedance inversion. The inversions with the 10 and 2 mS/m initial conductivity models show only minimal structural differences, when compared with the results of the reference starting model (with a 5 mS/m lower half-space). The 20mS/m case starts to introduce unwanted structure, whereas the 100 mS/m case lacks any semblance to the reference case. Both test scenarios point to the known fact that the choice of the background and starting model has an impact on the results of an inversion study.

The horizontal fields (E_x and E_y) obtained by a forward calculation of the final impedance in-

version model are used as input to evaluate the scaling factors. Data from all 25 receivers and all 15 frequencies are used, and the lowest frequency data were dropped due to poor fit. Table 1 gives a listing of the true and inverted scale factors. Field data (E_x and E_y) and the source scaling factors are input to the subsequent inversion. Figures 6 and 7 show the same depth level and vertical cut as in Figures 4 and 5. The final misfit is 0.63 (whereas 2.98 is the initial misfit). Both inversions reconstruct the L-shape horizontally reasonably accurately. The impedance inversion places the structure vertically more precisely and resolves the slope. The final impedance model produces higher differences in conductivity. The field-data model is smoother and less detailed. The base of the L-shape structure is not resolved as well as in the impedance case. The field data case resolves the change from the overlaying sediments into the
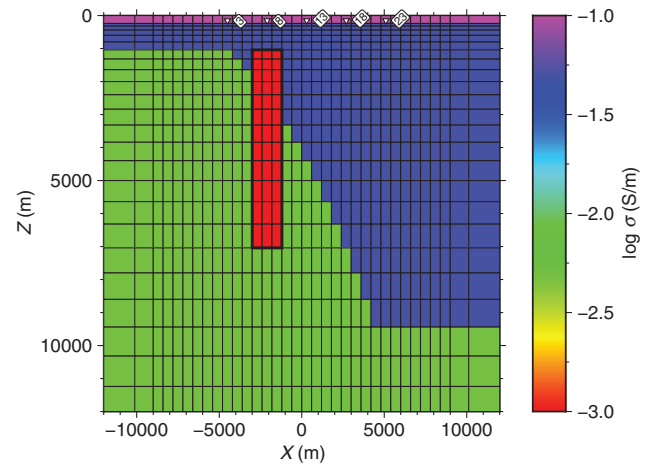

Figure 3. Vertical slice of the synthetic data model along the x-axis at $y = 0$.

Table 1. Scale factors used in the synthetic forward calculation and inverted factors.

| Frequency in Hz	$\alpha^{(1)}$	Inverted $\alpha^{(1)}$	$\alpha^{(2)}$	Inverted $\alpha^{(2)}$
0.100×10^1	$1.0 + i0.0$	$1.192 + i0.147$	$10.0 + i0.0$	$11.847 + i1.534$
0.611×10^0	$0.5 + i0.0$	$0.584 + i0.055$	$5.0 + i0.0$	$5.788 + i0.576$
0.373×10^0	$0.1 + i0.0$	$0.115 + i0.009$	$1.0 + i0.0$	$1.139 + i0.089$
0.228×10^0	$0.5 + i0.0$	$0.563 + i0.040$	$0.5 + i0.0$	$0.563 + i0.038$
0.139×10^0	$1.0 + i0.0$	$1.102 + i0.078$	$0.1 + i0.0$	$0.110 + i0.008$
0.848×10^{-1}	$5.0 + i0.0$	$5.355 + i0.382$	$0.5 + i0.0$	$0.536 + i0.042$
0.518×10^{-1}	$10.0 + i0.0$	$10.338 + i0.679$	$1.0 + i0.0$	$1.031 + i0.080$
0.316×10^{-1}	$5.0 + i0.0$	$5.123 + i0.267$	$5.0 + i0.0$	$5.110 + i0.313$
0.193×10^{-1}	$1.0 + i0.0$	$0.983 + i0.035$	$10.0 + i0.0$	$9.678 + i0.401$
0.118×10^{-1}	$0.5 + i0.0$	$0.487 + i0.007$	$5.0 + i0.0$	$4.783 + i0.088$
0.720×10^{-2}	$0.1 + i0.0$	$0.097 - i0.001$	$1.0 + i0.0$	$0.948 - i0.006$
0.439×10^{-2}	$0.5 + i0.0$	$0.502 - i0.019$	$0.5 + i0.0$	$0.495 - i0.017$
0.268×10^{-2}	$1.0 + i0.0$	$0.996 - i0.063$	$0.1 + i0.0$	$0.097 - i0.006$
0.164×10^{-2}	$5.0 + i0.0$	$0.517 - i0.389$	$0.5 + i0.0$	$0.505 - i0.040$
0.100×10^{-2}	$10.0 + i0.0$	Not used	$0.1 + i0.0$	Not used
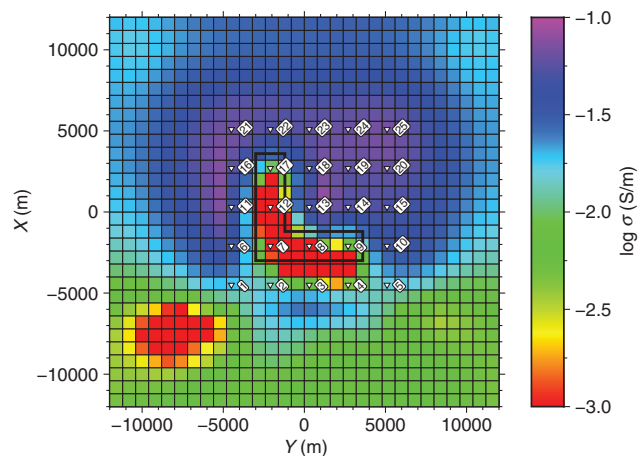
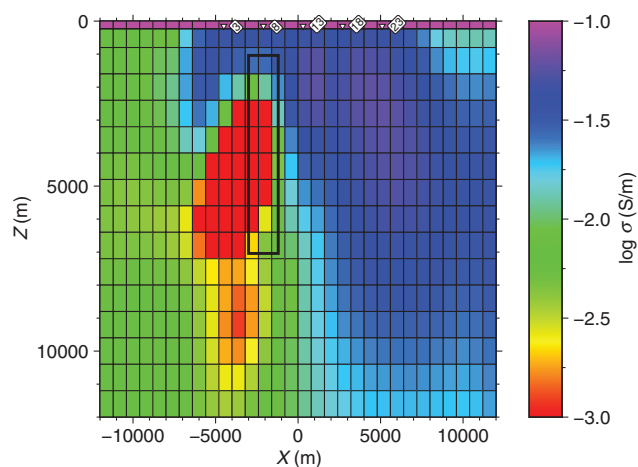Figure 4. Map view of the synthetic inversion model at 4 km depth. White triangles denote receiver positions.

Figure 5. Vertical slice of the synthetic inversion model along the x-axis at $y = 0$.
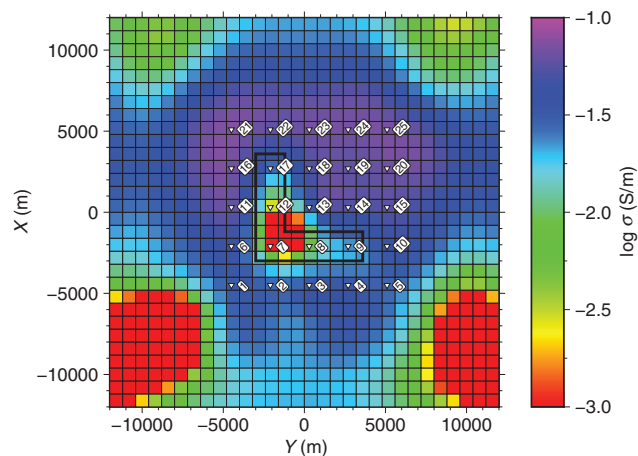

Figure 6. Map view of the synthetic field-data inversion model at a 4 km depth.

lower, less conductive basement at the foot of the slope. The inversions stopped after eight iterations for the impedance case and after 11 iterations for the electric-field data, respectively. Figure 8 shows the impedance transfer function for all used frequencies at receiver 8 (position $x = -2100$ m, $y = 300$ m). The splitting of the Z_{xy}- and Z_{yx}-component is caused by the east–west elongated lobe of the L–structure, and it is recovered by the inversion. Figure 9 shows the relative error of the absolute value of the E_x- and E_y-component for the used frequencies for the same receiver (no. 8). An observation is that Figures 8 and 9 do not show the same overall residual
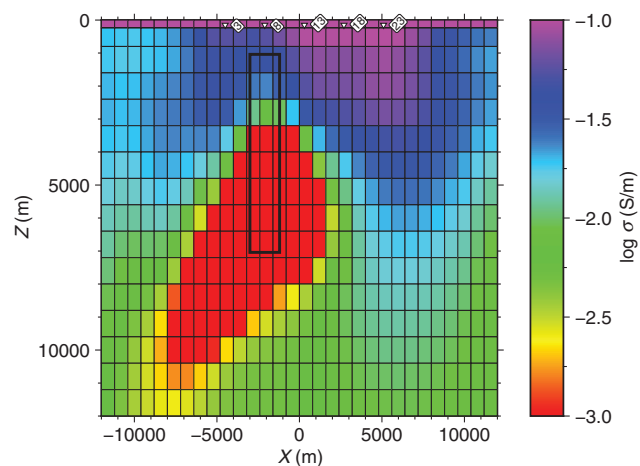

Figure 7. Vertical slice of the synthetic-field inversion model along the x-axis at $y = 0$.
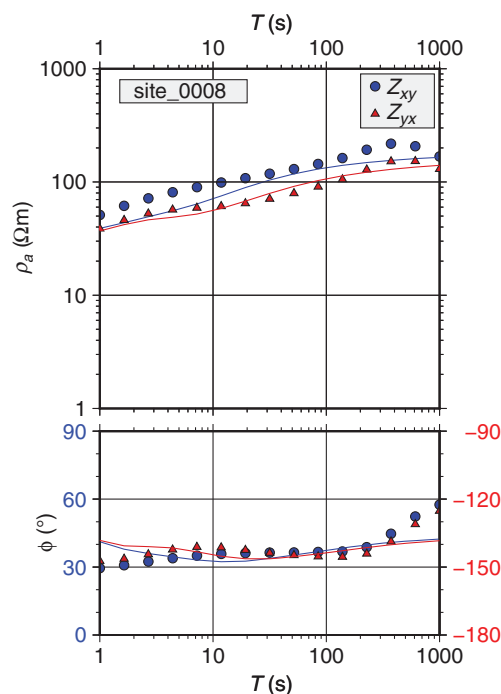

Figure 8. Overview of the impedance transfer function for receiver 8 (position $x = -2100$ m, $y = 300$ m) for the synthetic-data inversion. Input data are denoted by symbols, and inverted data are denoted by lines.

misfit trend, except for the lowest frequencies in which in both cases the misfit is higher. Both inversions share the same forward calculation. Given that, the deviation is likely caused by different sensitivities during the Jacobi matrix estimation.

REAL-DATA EXAMPLE

Survey area and layout

The observed data used in the real data example originate from the Nordkapp Basin in the Norwegian part of the Barents Sea. A phase of basement-involved extension during the end of early Jurassic triggered the uplift of salt deposited during Upper Carboniferous to Lower Permian times (see Nilsen et al., 1995). Salt diapirs have formed along the northeast-trending basin axis. The motivation to collect the data is to improve imaging of the vertical extent and shape of the salt. Natural variations of earth's electric and magnetic field have been recorded at 46 receiver locations, forming one 30 km line and a 3D staggered array on the seabed. The water depth ranges between 240 and 280 m. The receiver separation is 1.5 km along the long line and 3 km for the array (see also the map in Figure 10).

Impedance inversion

A subset of 19 receivers (marked by red circles around the position in Figure 10) is used in the further study. The selection is made on data quality and availability of synchronous recordings for the field inversion. Approximately six days of MT recording time are available, interrupted by a CSEM tow within the time span. All time series are low-passed from the original recording of 50 Hz to a frequency of 2 Hz. Single- and multiple-station time series processing (Egbert, 1997) is used to estimate MT impedances. Off-diagonal elements (Z_{xy}, Z_{yx}) of the MT impedance tensor at 10 frequencies between 4 and 500 s period are input to the inversion. Diagonal elements (Z_{xx}, Z_{yy}) are discarded because these elements for the most part of the data set are smaller than the error of the off-diagonal elements. The starting model has a 300 km span in all directions with a 500 m horizontal resolution in the central part. The vertical height of the cells is increasing exponentially with depth. The starting model contains of three layers: an air layer (10^{-7} S/m), a 270 m seawater layer (3.3 S/m), and a 0.1 S/m lower half-space. Like in the inversion of other geophysical data, the starting model has an influence on the final inversion model. Therefore, the choice of the lower half-space conductivity is not made by chance, but is a result of several previous test inversions leading to the lowest final misfit with a 0.1 S/m lower half-space starting model.

Figures 11 and 12 show a map view and vertical cuts from the impedance inversion conductivity model. The white line denotes the maximum horizontal salt extent derived from seismic data, but it is not used as prior information in the inverse process. Placement of the conductive structure coincides with the marine sediments in the basin. The extent of the resistive structures correlates well with the salt diapirs in the area. The top of the salt body is reconstructed by three resistive structures.

Intermediate conductive structures surround the core area toward the conductive sediments. The inversion converged at an rms value of 0.67 (with 5.35 before the first iteration). The data misfit is better for the receivers placed on the sediments. Receivers directly placed on the salt show higher misfit values (see the transfer function examples for receivers 6 and 10). The scattering in the shallow part of the model decreases with increasing depth where the model becomes smoother. The impedance-derived model suggests that the salt extends into the basement. To give an example of the data fit, Figures 13 and 14 show the inverted impedance transfer functions for receivers 6 and 10. The inversion cannot fully fit the strong component splitting caused by the salt observed at receiver 6. Receiver 10 is located further
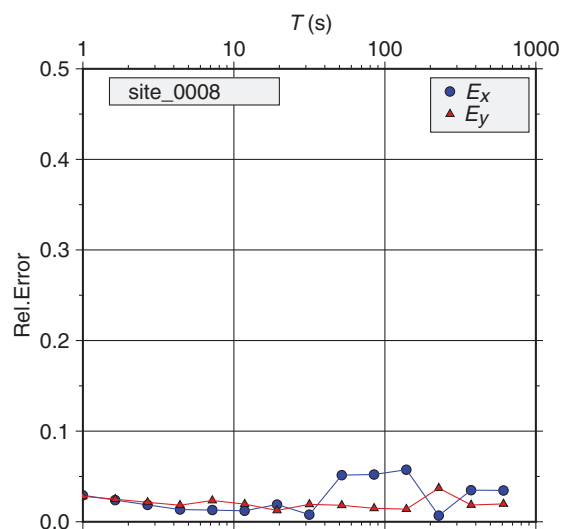

Figure 9. Overview of the synthetic direct-field inversion result for receiver 8 in form of relative error values.
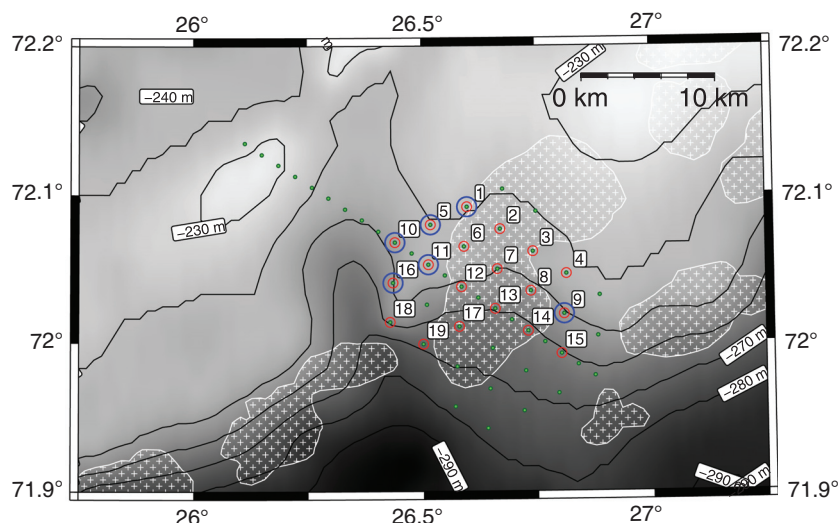

Figure 10. Survey map with maximum salt body extension (polygons filled with the white plus pattern), receiver locations and water-depth contours. A red circle around the receiver (green dots) indicates that data from this location are used in the impedance and field inversion. A blue circle indicates that this receiver is used in the source-scale estimation. Water-depth contours are given as black lines.

away from the salt and is mainly influenced by the marine sediments in the basin.

Inversion of the electric field

In preparation to the direct electric field inversion, a 2^{16}-sample (approximately 9 h) time window is selected and transformed to the frequency domain. The only additional processing step is a downward field continuation to the depth level of the deepest receiver. By doing this, the effect of the seawater acting as a low pass will be unified for all receivers. Fourier coefficients of the horizontal electric field (E_x and E_y) with the same set of frequencies as in the impedance inversion are selected as input to the inverse process.

The electric fields predicted from the final impedance inversion model for a subset of six (marked by a blue circle in Figure 10) receivers and the recorded data at these receivers are used in the

estimation of the source distribution. The choice of these particular receivers is based on the impedance inversion fit and the electric-field data quality. In addition, an error estimate (including receiver, frequency, and component specific misfits) from forward testing the scale factors in equation 12 is taken into account.
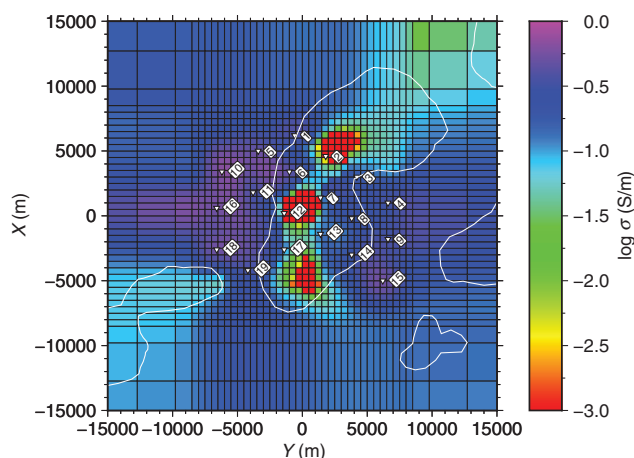

Figure 11. Map view shows the impedance-inversion model at depth between 850 and 1100 m with maximum salt-body outline and receiver locations.
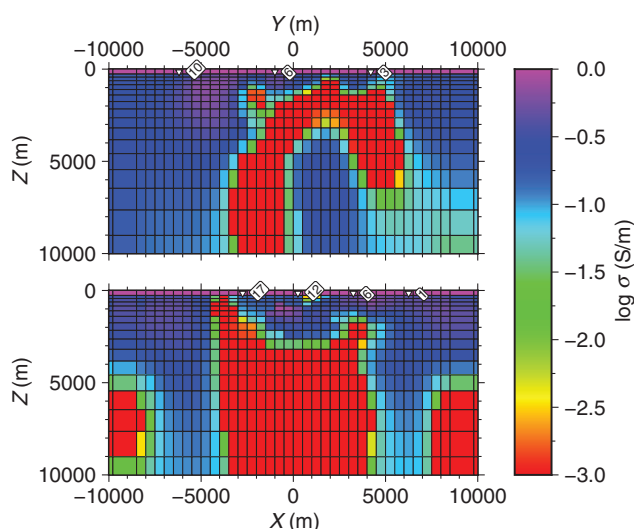

Figure 12. Vertical slices of the impedance inversion derived conductivity model. The top figure is a west−east cut along the *y*-axis located at $x = 3$ km. The bottom figure shows a south−north slice along *x*-axis at $y = -1$ km.
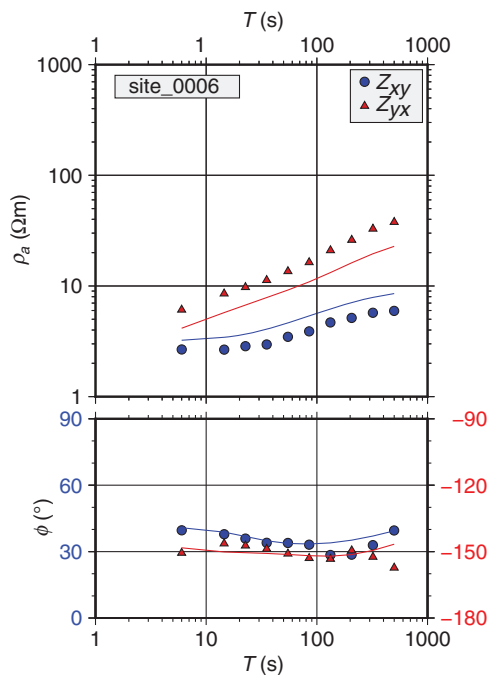

Figure 13. Overview of the impedance transfer function for receiver 6 for the observed data inversion. Input data are denoted by symbols, and inverted data are denoted by lines.
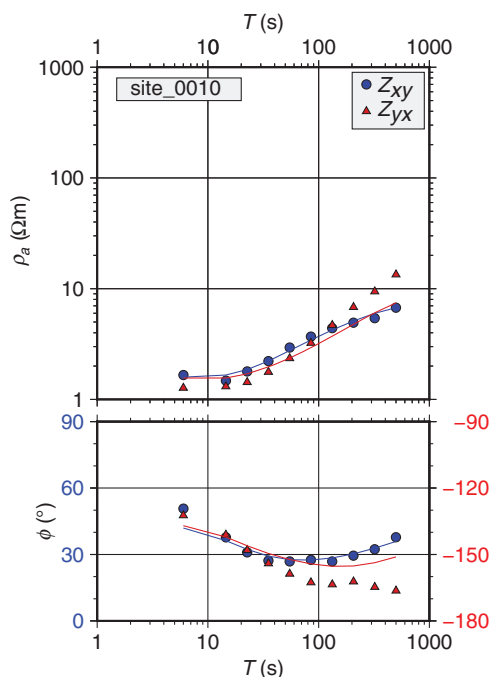

Figure 14. Overview of the impedance transfer function for receiver 10 for the observed data inversion. Input data are denoted by symbols, and inverted data are denoted by lines.

The source scaling factors plus the horizontal electric fields from all 19 stations are given as input to the direct-field inversion. The starting model is the same as in the impedance case. Figure 15 shows a map view at 850 m depth. Two orthogonal vertical sections of the model are shown in Figure 16. A conductive structure in a depth range from seabed to approximately 4 km depth is placed where the marine sediments are present. The salt is modeled as a compact body with little internal structure. Figures 17 and 18 show the relative errors for receivers 6 and 10. Both receivers exhibit a similar uniform misfit level for the different frequencies without strong trends. The field inversion leads to a compact salt body with a possible interpretation that it is not connected to the base salt. The final rms value is at 1.63 (with an initial misfit value of 2.98).

The differences, when compared with the impedance inversion, in the place and shape of the resistive salt structure, are most likely

caused by a different characteristic of the sensitivities. An insufficient quality of the source estimation, caused by noise in the data, may prevent the direct-field inversion from a better fit. Both inversions are able to detect the influence of high-resistive structures (neighboring salt diapirs) that are outside of the receiver array. A point to note is that both inversions (impedance and direct-field type, synthetic and real data) get close to the final misfit level after 4–5 iterations, with only minor changes at later iterations.

DISCUSSION AND FUTURE WORK

Running an inversion with field data can be advantageous for a couple of reasons. Most important to mention is the simplification (see Appendix B) within the estimation of the sensitivity matrix
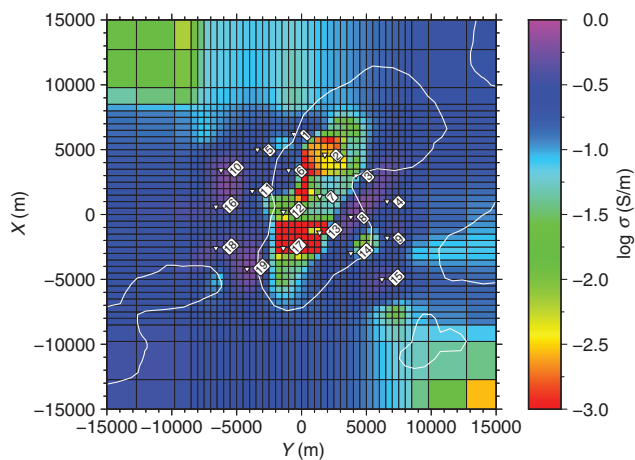

Figure 15. Map view shows the direct-field data inversion model at depth between 850 and 1100 m with maximum salt-body outline and receiver locations.
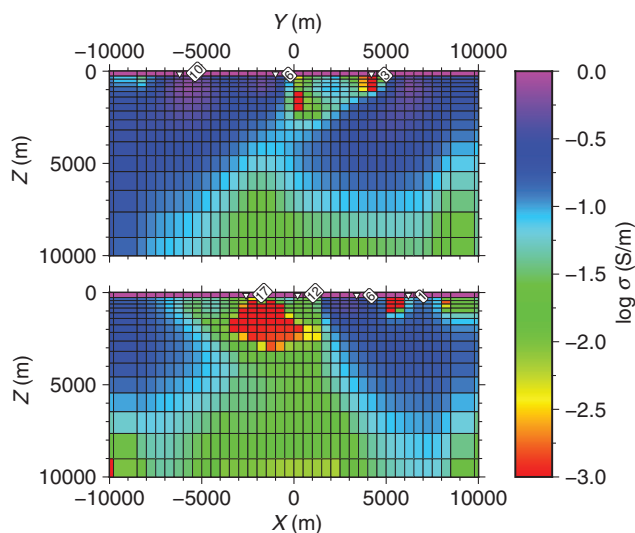

Figure 16. Vertical slices of the conductivity model derived by the inversion of the observed field data. Top figure shows a west−east cut, located at $x = 3$ km along the y-axis, and the bottom figure shows a south−north slice along the x-axis at $y = -1$ km.
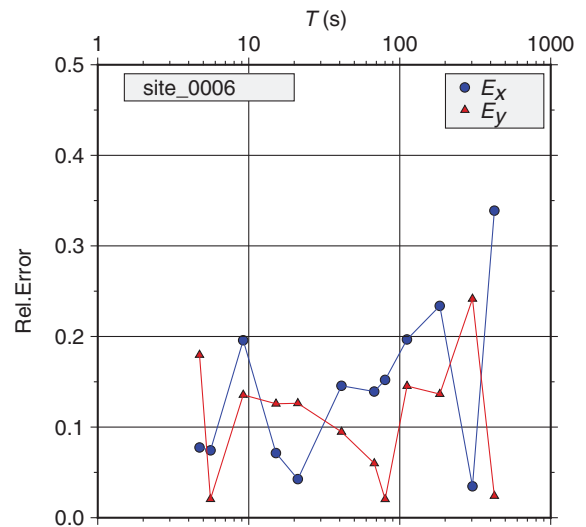

Figure 17. Overview of the observed direct-field inversion result for receiver 6 given as the relative error of the absolute value of the datum.
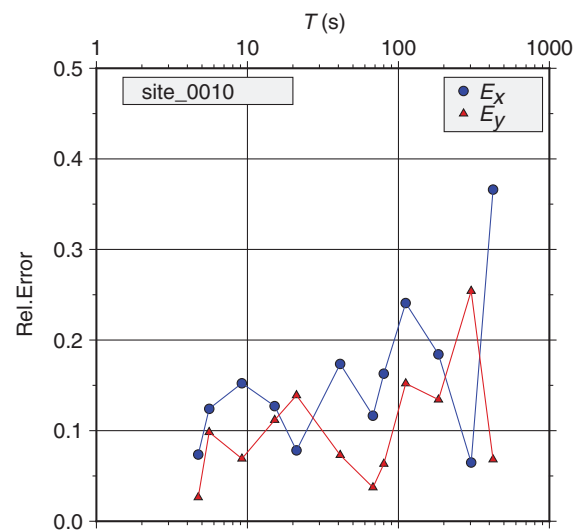

Figure 18. Overview of the observed direct-field inversion result for receiver 10 given as the relative error of the absolute value of the datum.

elements. The complicated expression for the derivative of the data (impedance tensor elements) with respect to the field solution is reduced to the sum of the contributions of the two EM field polarizations. This reduction in nonlinearity is beneficial to the inverse process because it helps to converge faster with less local minima in the objective function.

The elements of the impedance tensor reflect the dimensionality of the subsurface. The diagonal elements become only significant in a true 3D situation. Including the Z_{xx} and Z_{yy} data is not trivial in a data set with mixed (1D, 2D, and 3D) structural dimensionality, as the diagonal components are zero or very small for parts of the input data. The field approach handles the dimensionality of the subsurface response in a general way, without introducing interpretative information (in form of data weights) to the input data.

Applying the novel approach allows to use existing data in an alternative way. The field inversion can be used to confirm or challenge the results from an impedance inversion. The synthetic data example results of the impedance and field inversion are similar. The impedance inversion gives a better vertical placement and shape of the L–structure, whereas the field inversion slightly better separates the L-structure from the slope and resolves the base of the slope. In the real-data example, the differences are more pronounced. The field-data inversion resolves a sharper, more continuous salt structure, whereas the conductive marine sediments are mapped similarly (with exceptions close to receivers 1 and 14) for both inversion types. The vertical distribution of conductivities for the salt structure is different in the models. The field inversion produces a resistive structure that is confined to the overburden. The impedance-derived model shows a deeper buried massive resistive structure with a smaller structure above, close to the seabed.

One critical point to mention is that the field approach uses the measured data almost raw; this demands high-quality data. The effect of outliers, coherent or local noise in the data, is introduced to the field inversion unfiltered, and therefore it is influencing the inversion results. The impedance data processing helps to estimate robust data, which then are handed over to the inverse process, helping to reduce the influence of noise. In the synthetic example shown above, the impedance and the electric field inversion are able to reconstruct the initial conductivity model in presence of incoherent noise. In the real-data example, the quality of the data is generally good and the overall reconstructed models are comparable. In an onshore setting with, for example, static shift and/or cultural noise, this might not be the case.

The impedance and field inversion use the same forward calculation method (the finite-volume approach), and therefore they share the same limitations that arise from it. The scattered field approach allows a simplification in the handling of the sources of the EM field, by solving the primary field contribution in a separate background model. In a setting with a varying model surface, especially in the presence of strong bathymetry, a total-field finite-element, or finite-difference-based forward algorithm probably gives a more accurate modeling of the EM fields.

One point to mention is that the inversion of the field components requires the estimation of the source scaling factors, which is an additional step in the preparation of the inversion input data. With the method described above, the source estimation is dependent on a conductivity model (found by impedance inversion) explaining at least parts of data. By that, the direct-field approach cannot be classified as fully independent, but it is a hybrid inversion. Future work should therefore be directed at alternative methods for the source

field estimation either by estimation from the data or by direct measurement. In addition to separate inversions, it is also possible to combine the two inversion types. For example, run a supplemental field inversion from the final impedance inversion result as the starting model. The results of such combined inversions will be highly dependent on the preceding inversion.

CONCLUSION

In this paper, we introduce an approach to invert MT electric-field data in a Gauss-Newton-like inversion scheme. Conventional MT inversion seeks to reconstruct the subsurface electric conductivity structure with the help of impedance data. The use of impedances is justified by the fact that no further information about the distribution of the source field is needed. The estimation of the impedance tensor elements includes a deconvolution operator that increases the nonlinearity of the inverse problem. The novel approach circumvents the complicated impedance formulation by directly using the observed electric-field data, but it demands knowledge of the source distribution. A least-squares scheme is used to estimate the source scaling factors from the unit source response of a conductivity model.

The ability of the inversion scheme to reconstruct the 3D conductivity structures from electric-field data is tested on synthetic and observed data, both set in a marine environment. In the synthetic data example, the test model is reproduced accurately for both inversion types. The field-data inversion produces a slightly smoother result. At the same time, the method to estimate the source distribution is verified. Both types of inversions share the same finite-volume scattered field forward calculation. A test to investigate the influence of the background model (needed in the forward calculation) and starting model on the inversion result is conducted for the synthetic data example. It shows that very off-valued background/starting models introduce conductivity artifacts in the inversion results and lead to higher data-misfit values.

The real data originate from a basin in the Norwegian Barents Sea. Here, the impedance and field-data inversions produce less similarity in the final models. Although the extent of the conductive marine sediments is modeled comparably, the shape and composition of a salt body shows deviations. The electric-field inversion example produces a more focused model with a higher structured salt shape. The vertical section reveals a large resistive structure in the impedance case, in which the field-data inversion shows a compact structure only close to the seabed. The receiver specific misfit in the impedance case reveals that this inversion is more problematic in locations directly above the salt structure. Because the field-data inversion uses almost unprocessed electric-field data, it demands high quality. Outliers or noise will influence the electric-field inversion directly.

The synthetic example exhibits no, and the real-data example exhibits only mild seafloor topography. In the presence of very strong bathymetry, the used scattered-field forward calculation will give inaccuracies. In the ill-posed setting of MT inversion, the necessary regularization and model discretization set an additional limit to the resolvability of small-scale conductivity contrasts. The simplification in the direct-field inversion comes at the cost of knowledge of the source distribution, which is an additional step in the input data preparation. Because the described scheme of the source estimation is dependent on a prior impedance inversion, it cannot be seen a fully stand-alone inversion but as a hybrid approach.

APPENDIX A

JACOBI DERIVATION

The following derivation of the Jacobi matrix elements can be found in greater detail in the Ph.D. thesis of Meqbel (2009). In general, the Jacobi or sensitivity matrix is defined as

$$\mathbf{J} = \frac{\partial \mathbf{F}(\mathbf{m})}{\partial \mathbf{m}} = \frac{\partial \psi(\mathbf{e}(\mathbf{m}))}{\partial \mathbf{m}}, \tag{A-1}$$

where $\mathbf{F}(\mathbf{m})$ is the predicted data, which itself is a function of the electric-field solution, which is again a function of the model parameters. The function ψ includes interpolation of the electric-field solution from the grid nodes to the receiver position, calculation of magnetic fields, and calculation of the data itself (e.g., Z_{xy}). Equation A-1 becomes

$$\mathbf{J} = \frac{\partial \psi}{\partial \mathbf{e}} \frac{\partial \mathbf{e}}{\partial \mathbf{m}} + \frac{\partial \psi}{\partial \mathbf{m}}. \tag{A-2}$$

The trailing term is zero in our implementation. The exact formulation of the $\partial \psi / \partial \mathbf{e}$ term strongly depends on the interpolation and predicted data calculation of the used algorithms. The $\partial \mathbf{e} / \partial \mathbf{m}$ term can be found by taking the partial derivative of equation 5 with respect to the model. This leads to

$$\frac{\partial \mathbf{A}}{\partial \mathbf{m}} \mathbf{e} + \mathbf{A} \frac{\partial \mathbf{e}}{\partial \mathbf{m}} = \frac{\partial \mathbf{b}}{\partial \mathbf{m}}, \tag{A-3}$$

$$\frac{\partial \mathbf{e}}{\partial \mathbf{m}} = \mathbf{A}^{-1} \left(-\frac{\partial \mathbf{A}}{\partial \mathbf{m}} \mathbf{e} + \frac{\partial \mathbf{b}}{\partial \mathbf{m}} \right). \tag{A-4}$$

Put back into equation A-2, we have found an expression for the Jacobi matrix:

$$\mathbf{J} = \frac{\partial \psi}{\partial \mathbf{e}} \mathbf{A}^{-1} \left(-\frac{\partial \mathbf{A}}{\partial \mathbf{m}} \mathbf{e} + \frac{\partial \mathbf{b}}{\partial \mathbf{m}} \right). \tag{A-5}$$

To calculate all elements of the Jacobi matrix $\mathbf{M}$ (number of model parameters), forward calculations are necessary. In 3D MT, the number of model parameters is higher than the number of data points, using the transposed Jacobian is therefore much more efficient:

$$\mathbf{J}^T = \left(-\frac{\partial \mathbf{A}}{\partial \mathbf{m}} \mathbf{e} + \frac{\partial \mathbf{b}}{\partial \mathbf{m}} \right)^T (\mathbf{A}^{-1})^T \left(\frac{\partial \psi}{\partial \mathbf{e}} \right)^T. \tag{A-6}$$

APPENDIX B

FULL-IMPEDANCE EXPRESSION

Here, we give the full expression of the derivative of the first off-diagonal element of the impedance tensor:

$$Z_{xy} = \frac{E_x^{(2)} H_x^{(1)} - E_x^{(1)} H_x^{(2)}}{H_x^{(1)} H_y^{(2)} - H_x^{(2)} H_y^{(1)}}. \tag{B-1}$$

We take the derivative with respect to the electric-field solution and sort for the two polarizations:

$$
\begin{aligned}
\frac{\partial \psi}{\partial \mathbf{e}} = \frac{\partial Z_{xy}}{\partial e_k} = &\left[\frac{\partial E_x^{(1)}}{\partial e_k} H_x^{(2)} (H_x^{(2)} H_y^{(1)} - H_x^{(1)} H_y^{(2)}) \right. \\
&+ \frac{\partial H_x^{(1)}}{\partial e_k} H_x^{(2)} (E_x^{(1)} H_y^{(2)} - E_x^{(2)} H_y^{(1)}) \\
&+ \frac{\partial H_y^{(1)}}{\partial e_k} H_x^{(2)} (E_x^{(2)} H_x^{(1)} - E_x^{(1)} H_x^{(2)}) \\
&+ \frac{\partial E_x^{(2)}}{\partial e_k} H_x^{(1)} (H_x^{(1)} H_y^{(2)} - H_x^{(2)} H_y^{(1)}) \\
&+ \frac{\partial H_x^{(2)}}{\partial e_k} H_x^{(1)} (E_x^{(2)} H_y^{(1)} - E_x^{(1)} H_y^{(2)}) \\
&\left. + \frac{\partial H_y^{(2)}}{\partial e_k} H_x^{(1)} (E_x^{(1)} H_x^{(2)} - E_x^{(2)} H_x^{(1)}) \right] \\
&/ (H_x^{(1)} H_y^{(2)} - H_x^{(2)} H_y^{(1)})^2
\end{aligned} \tag{B-2}
$$

In the case in which we use, for example, the E_x-component in the electric-field data inversion, this reduces to

$$\frac{\partial \psi}{\partial \mathbf{e}} = \frac{\partial E_x}{\partial e_k} = \frac{\partial E_x^{(1)}}{\partial e_k} + \frac{\partial E_x^{(2)}}{\partial e_k}. \tag{B-3}$$

REFERENCES

Avdeev, D. B., 2005, Three-dimensional electromagnetic modeling and inversion from theory to application: Surveys in Geophysics, **26**, 767–799, doi: 10.1007/s10712-005-1836-x.

Constable, S., 2010, Ten years of marine CSEM for hydrocarbon exploration: Geophysics, **75**, no. 5, 75A67–75A81, doi: 10.1190/1.3483451.

Constable, S., and L. J. Srnka, 2007, An introduction to marine controlled-source electromagnetic methods for hydrocarbon exploration: Geophysics, **72**, no. 2, WA3–WA12, doi: 10.1190/1.2432483.

Egbert, G. D., 1997, Robust multiple-station magnetotelluric data processing: Geophysical Journal International, **130**, 475–496, doi: 10.1111/j.1365-246X.1997.tb05663.x.

Meqbel, N., 2009, The electrical conductivity structure of the Dead Sea Basin derived from 2D and 3D inversion of magnetotelluric data: Ph.D. thesis, Freie Universität Berlin.

Mittet, R., F. Maaø, O. M. Aakervik, and S. Ellingsrud, 2005, A two-step approach to depth migration of low frequency electromagnetic data: 75th Annual International Meeting, SEG, Expanded Abstracts, 522–525.

Nilsen, K. T., J. T. Johansen, and B. C. Vendeville, 1995, Influence of regional tectonics on halokinesis in the Nordkapp Basin, Barents Sea, in Salt tectonics: A global perspective: AAPG Memoir, 413–436.

Schenk, O., and K. Gärtner, 2004, Solving unsymmetric sparse systems of linear equations with PARDISO: Future Generation Computer Systems, **20**, 475–487, doi: 10.1016/j.future.2003.07.011.

Schmucker, U., 1970, Anomalies of geomagnetic variations in the southwestern United States: University of California Press.

Siripunvaraporn, W., G. Egbert, Y. Lenbury, and M. Uyeshima, 2005, Three-dimensional magnetotelluric inversion: Data-space method: Physics of the Earth and Planetary Interiors, **150**, 3–14, doi: 10.1016/j.pepi.2004.08.023.

Soyer, W., and H. Brasse, 2001, A magneto-variation array study in the central Andes of N Chile and SW Bolivia: Geophysical Research Letters, **28**, 3023–3026, doi: 10.1029/2000GL012095.

Ward, S. H., and G. W. Hohmann, 1988, Electromagnetic theory for geophysical applications, *in* M. N. Nabighian, ed., Electromagnetic methods in applied geophysics: SEG, 131–311.

Weiss, C. J., and S. Constable, 2006, Mapping thin resistors and hydrocarbons with marine EM methods. Part II: Modeling and analysis in 3D: Geophysics, **71**, no. 6, G321–G332, doi: 10.1190/1.2356908.

Wiik, T., K. Hokstad, B. Ursin, and L. Mütschard, 2013, Joint contrast source inversion of marine magnetotelluric and controlled-source electromagnetic data: Geophysics, **78**, no. 6, E315–E327, doi: 10.1190/geo2012-0477.1.